APSIPA Transactions on Signal and Information Processing, 2025, 14, e29

Original Paper

Nested Frequency Diverse Array for Co-located MIMO Radar using Grid-free DOA and Range Estimation Method

Beizuo Zhu[1*], Kazunori Hayashi[2] and Hiroki Mori[3]

[1] *Graduate School of Informatics, Kyoto University, Kyoto, Japan*
[2] *Institute for Liberal Arts and Sciences, Kyoto University, Kyoto, Japan*
[3] *Toshiba Corporation, Japan*

ABSTRACT

The paper considers the design of frequency diverse array (FDA) for co-located multi-input multi-output (MIMO) radar employing a joint grid-free direction of arrival (DOA) and range estimation method, and proposes a design approach using a nested array as the physical antenna array. Specifically, an inner uniform linear subarray of the nested array is employed for the transmitting array, while the entire nested array serves as the receiving array. Moreover, a grid-free method using atomic norm minimization (ANM) is employed to realize joint DOA and range estimation, making full use of the extended virtual array aperture by the nested array. One of key features of the proposed nested FDA MIMO radar is that it enables fine-tuning of the balance between the DOA and range estimation performance by adjusting the level of the nested array. The numerical results validate the effectiveness of the proposed approach, highlighting the feasibility of controlling the balance between the DOA and range estimation performance by adjusting

*Corresponding author: zhu.beizuo.54t@st.kyoto-u.ac.jp. This work was supported by JST, the establishment of university fellowships towards the creation of science technology innovation, Grant Number JPMJFS2123.

Received 14 January 2025; revised 16 July 2025; accepted 10 August 2025
ISSN 2048-7703; DOI 10.1561/116.20250002

the level of the nested array. Moreover, the proposed nested FDA MIMO radar outperforms the FDA MIMO radar with a uniform linear array (ULA) in terms of both DOA and range estimation performance for the appropriate choice of the level.

Keywords: Frequency diverse array, nested array, atomic norm minimization, MIMO radar

1 Introduction

Frequency diverse array (FDA) for multi-input multi-output (MIMO) radar [1, 18], which can achieve joint direction of arrival (DOA) and range estimation, has received much attention in recent years. Several subspace based algorithms for the FDA MIMO radar have been proposed, such as the multiple signal classification (MUSIC) based algorithm [26], the parallel factor analysis (PARAFAC) based algorithm [31], and the estimation of signal parameters via rotational invariance techniques (ESPRIT) based algorithm [27]. Moreover, a sparse array has been introduced into the FDA MIMO radar in [5] to extend the aperture of the array. However, those algorithms generally require a large number of snapshots to accurately estimate the correlation matrix of the received signal, and thus a large estimation delay, which might not be acceptable in some applications.

In order to reduce the required number of snapshots, a compressed sensing (CS) [4, 20] based approach has been introduced to the problem of joint DOA and range estimation with the FDA MIMO radar, as in the case of the conventional DOA estimation problem. For example, a sparse learning-based target parameter estimation method is proposed in [9], where a hybrid algorithm is designed to adaptively select the best algorithm based on the number of snapshots and targets, which can achieve estimation performance close to the CramerRao lower bound (CRLB) in various scenarios. Graph signal processing (GSP) has been introduced into FDA-MIMO radar in [23], and a joint DOA and range estimation algorithm based on graph Fourier transform (GFT) is proposed. In the method, the graph model of the signal is first constructed by the adjacency matrix, then GFT is performed to extract the target information, and finally the DOA and range estimates of the target are obtained through spectrum peak search. In general, CS based methods require small number of snapshots, but the array structure of the methods is commonly limited to the uniform linear array (ULA), and they suffer from the grid mismatch problem due to the bias between the predefined discrete sampling grid and the actual signal parameter, which degrades the estimation performance.

A grid-free CS based algorithm using two dimensional (2D) atomic norm minimization (ANM) [19] has been proposed to overcome the grid mismatch problem in the conventional CS approach. Based on the signal model of the FDA MIMO radar, the 2D ANM problem is established by using vectorization of the received signal, and the ANM problem is transformed into a semidefinite programming (SDP) problem, which can be solved efficiently using the accelerated proximal gradient (APG) method. Moreover, the idea of the sparse array has been introduced in [25] to reduce the computational complexity of the method in [19] with a negligible performance degradation, assuming that a common physical antenna array is used for both the transmission and the reception (i.e., co-located MIMO radar). In the method, the ULA is employed as the physical array, and the entire ULA is used as the transmitting array, while the sparse array, which is composed by thinning out some elements of the ULA, is utilized as the receiving array. In addition, ANM has been applied for the FDA radar using a coprime array in [15] for joint DOA and range estimation, where the transmitting antenna is restricted to be a single element antenna, which might degrade the estimation performance. To the best of our knowledge, however, no CS based FDA MIMO radar, which can employ the sparse array as the physical array, has been proposed in the literature.

Recently, data-driven deep learning approaches have obtained growing interest in various fields, including radar signal processing. For example, double deep Q-network (DDQN) [32, 6] and deep deterministic policy gradient (DDPG) [24] have shown promising performance in radar applications. Moreover, recent works have applied deep reinforcement learning (DRL) to optimize wireless systems under practical hardware constraints. For example, a DRL-based precoding framework for multi-RIS-aided multiuser downlink systems with practical phase shift models has been proposed in [2], where a DDPG algorithm jointly optimizes transmitter precoding and RIS phase shifts to maximize spectral efficiency. However, they typically require large amounts of training data and offline training, which can be impractical in real-time applications or time-varying environments.

In this paper, we consider introducing a sparse array as the physical array of the co-located FDA MIMO radar using the 2D ANM. Unlike the FDA MIMO radar in [25], where the idea of a sparse array is used to reduce computational complexity, the purpose of this study is to improve the estimation performance of the method in [19] taking advantage of the extended virtual array aperture. As the configuration of the physical sparse array, we propose to employ a nested array [16], since its inner subarray has a ULA structure, which enables us to solve the 2D ANM problem by taking advantage of Vandermonde decomposition of the multilevel Toeplitz matrix [30]. Meanwhile, the entire nested array is used as the receiving array to achieve better DOA estimation performance. The proposed nested FDA MIMO radar can control the balance between DOA and range estimation performance by selecting the

level of the nested array. This is because it can change the number of inner ULA elements and the virtual array aperture, which govern the range estimation performance and the DOA estimation performance, respectively. The numerical results demonstrate the validity of the proposed approach and the feasibility of controlling the balance between DOA and range estimation performance by adjusting the level of the nested array. Moreover, the proposed nested FDA MIMO radar with 1-level nested array can significantly outperform the CS based state-of-the-art methods using the ULA, especially in DOA estimation performance, given the appropriate choice of parameters.

The main contributions of the paper can be summarized as follows:

- The sparse array is employed as the physical array in FDA MIMO radar based on CS for the first time to extend the array aperture, while requiring a small number of snapshots.
- The level of the nested array is introduced as a tunable parameter to optimize the trade-off between the DOA and range estimation performance, which allows adaptation to different application requirements.
- The proposed nested FDA MIMO radar significantly outperforms the CS based state-of-the-art methods, especially in DOA estimation performance.

In the rest of paper, $\mathbb{N}$ and $\mathbb{C}$ denote sets of all natural numbers and complex numbers, respectively. We use lower-case bold characters to denote column vectors and upper-case bold characters for matrices. $\mathbf{1}_M$ and $\mathbf{0}_M$ are all-one and all-zero vectors of size $M \times 1$, respectively. $(\cdot)^T$ and $(\cdot)^H$ are the transpose and conjugate transpose of a matrix or vector, respectively. $(\cdot)^{-1}$ and $(\cdot)^\dagger$ denote inverse and pseudo-inverse of a matrix, respectively. $\oplus$, $\otimes$, and $\odot$ represent Hadamard product, Kronecker product, and Khatri-Rao product, respectively. $\mathrm{tr}(\cdot)$ and $\|\cdot\|_F$ denote the trace and Frobenius norm, respectively. For a matrix $\mathbf{A}$, $\mathrm{diag}_k(\mathbf{A})$ denotes a column vector obtained by extracting the k-th diagonal elements of $\mathbf{A}$. $E[\cdot]$ denotes the mathematical expectation operator.

2 System Model

We consider an FDA for co-located MIMO radar as depicted in Figure 1, where N physical antenna elements are arranged in a linear array. The location set of the antenna elements is defined as

$$\Phi = \{\phi_0 d, \phi_1 d, \ldots, \phi_{N-1} d\}, \tag{1}$$

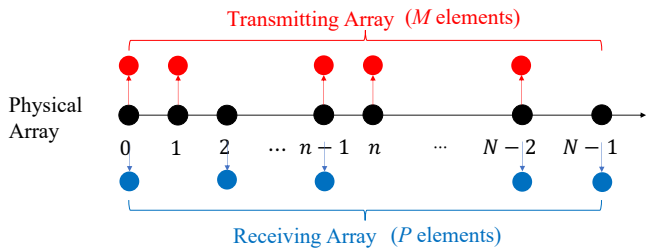

Figure 1: An example of FDA for co-located MIMO radar.

where $\phi_n \in \mathbb{N}$ $(n = 0, 1, \ldots, N-1)$ and d denotes unit spacing between antenna elements. Without loss of generality, we assume the 0-th antenna element is located at the origin, and set $\phi_0 = 0$. We use subarrays of this physical array having M $(\leq N)$ and P $(\leq N)$ elements for the transmitting array and the receiving array, respectively. In Figure 1, examples of the transmitting and the receiving arrays, which are composed by selecting some antenna elements from the physical array, are also depicted with red and blue colors.

The location sets of transmitting array and the receiving array are defined as

$$\Phi_{\mathrm{t}} = \{\alpha_0 d, \alpha_1 d, \ldots, \alpha_{M-1} d\} \subseteq \Phi, \tag{2}$$

$$\Phi_{\mathrm{r}} = \{\beta_0 d, \beta_1 d, \ldots, \beta_{P-1} d\} \subseteq \Phi, \tag{3}$$

respectively, where $\alpha_m d$ is the location of the m-th transmitting antenna, $\beta_p d$ is that of the p-th receiving antenna, and we assume $\alpha_0 = \beta_0$. Since we employ FDA with uniform frequency shift, the carrier frequency at the m-th transmitting antenna is given by

$$f_m = f_0 + \alpha_m \Delta f, \ \ (m = 0, 1, \ldots, M-1), \tag{4}$$

where f_0 denotes the carrier frequency at the 0-th transmitting antenna and $\Delta f (\ll f_0)$ is the frequency shift corresponding to the unit antenna spacing d. To avoid the ambiguity in the DOA estimation, d is set to be the half of the smallest wavelength among the transmitted signals as

$$d = \frac{c}{2(f_0 + \alpha_{M-1}\Delta f)}, \tag{5}$$

where c is the speed of light.

Based on (4), the transmitted signal by the m-th transmitting antenna element is given as

$$x_m(t) = \phi_m(t) e^{j2\pi(f_0 + \alpha_m \Delta f)t}, \tag{6}$$

where $\phi_m(t)$ is the orthogonal baseband waveform with duration of T from the m-th transmitting antenna, which has properties of [3]

$$\int_0^T \phi_{m_1}(t)\phi_{m_2}^*(t-\tau)dt = \begin{cases} 0 & (m_1 \neq m_2) \\ 0 & (m_1 = m_2, \tau \neq 0) \\ 1 & (m_1 = m_2, \tau = 0) \end{cases}. \tag{7}$$

Note that, in practice, this condition is difficult to achieve perfectly due to hardware limitations such as finite chip length, imperfect synchronization, and hardware nonlinearity. This may lead to partial loss of orthogonality, resulting in a slight degradation of estimation performance. If the non-ideal waveform orthogonality becomes a serious limiting factor in implementation, time division multiplexing (TDM) signaling can alternatively be used to ensure strict orthogonality by assigning separate time slots to different transmitting antennas.

Assume that there are K targets in the far field from the FDA with DOA and range pairs of (θ_k, r_k), $(k = 0, 1, \cdots, K-1)$ with respect to the 0-th transmitting and receiving antenna. The reference time delay of the k-th target is defined as the time delay from the 0-th transmitting antenna to the 0-th receiving antenna, namely $\tau_{0,0,k} = 2r_k/c$. Thus, the relative time delay of the signal from the m-th transmitting antenna and p-th receiving antenna with respect to the reference time delay can be expressed as

$$\tau_{m,p,k} = \tau_{0,0,k} - \left(\frac{\alpha_m d \sin\theta_k}{c} + \frac{\beta_p d \sin\theta_k}{c}\right) \tag{8}$$

due to the far field assumption.

If we focus only on the k-th target and ignore the additive noise for a while, the corresponding received signal at the p-th receiving antenna is given by

$$\begin{aligned} x_{p,k}(t) &= \sum_{m=0}^{M-1} x_{m,p,k}(t) \\ &= \sum_{m=0}^{M-1} \phi_m(t-\tau_{m,p,k}) e^{j2\pi(f_0+\alpha_m\Delta f)(t-\tau_{m,p,k})}, \end{aligned} \tag{9}$$

where $x_{m,p,k}(t)$ is the received signal corresponding to the k-th target at the p-th receiving antenna originally from the m-th transmitting antenna. At the p-th receiving antenna, in order to extract the signal from the m-th transmitting antenna, we perform down-conversion corresponding to the carrier frequency and frequency shift, which results in

$$\hat{y}_{m,p,k}(t) = e^{-j2\pi(f_0+\alpha_m\Delta f)t} x_{p,k}(t).$$

Then, we perform matched filtering given by

$$\begin{aligned}\bar{y}_{m,p,k}(\tau) &= \int_0^T \phi_m^*(t-\tau)\,\hat{y}_{m,p,k}(t)dt \\ &\approx \sum_{m'=0}^{M-1} e^{-j2\pi(f_0+\alpha_{m'}\Delta f)\tau_{m',p,k}} e^{j2\pi(\alpha_{m'}-\alpha_m)\frac{\Delta f T}{2}} \\ &\quad \cdot \int_0^T \phi_m^*(t-\tau)\,\phi_{m'}(t-\tau_{m',p,k})dt.\end{aligned}$$

The detailed derivation can be found in Appendix A.1. Based on the orthogonality property of the baseband waveform $\phi_m(t)$ in (7), the output of the matched filter is developed as

$$\begin{aligned}\bar{y}_{m,p,k}(\tau) &= e^{-j2\pi(f_0+\alpha_m\Delta f)\tau_{m,p,k}} \int_0^T \phi_m^*(t-\tau)\,\phi_m(t-\tau_{m,p,k})dt \\ &= \begin{cases} e^{-j2\pi(f_0+\alpha_m\Delta f)\tau_{m,p,k}} & (\tau=\tau_{m,p,k}) \\ 0 & (\tau\neq\tau_{m,p,k}) \end{cases}.\end{aligned}$$

It can be found that, if and only if $\tau = \tau_{m,p,k}$ is satisfied, the matched filter output has non-zero output expressed as

$$\begin{aligned}y_{m,p,k} &= \bar{y}_{m,p,k}(\tau_{m,p,k}) \\ &= e^{-j2\pi f_0\frac{2r_k}{c}} e^{j2\pi(f_0+\alpha_m\Delta f)\frac{\alpha_m d\sin\theta_k}{c}} e^{j2\pi(f_0+\alpha_m\Delta f)\frac{\beta_p d\sin\theta_k}{c}} \\ &\quad \cdot e^{-j2\pi\alpha_m\Delta f\frac{2r_k}{c}}.\end{aligned} \tag{10}$$

Because we assume $\Delta f \ll f_0$, we have

$$\begin{aligned}e^{j2\pi(f_0+\alpha_m\Delta f)\frac{\alpha_m d\sin\theta_k}{c}} &\approx e^{j2\pi f_0\frac{\alpha_m d\sin\theta_k}{c}} \\ e^{j2\pi(f_0+\alpha_m\Delta f)\frac{\beta_p d\sin\theta_k}{c}} &\approx e^{j2\pi f_0\frac{\beta_p d\sin\theta_k}{c}}.\end{aligned}$$

Besides, if we define $\xi_k = e^{-j2\pi f_0\frac{2r_k}{c}}$ depending only on the target, the received signal after matched filtering can be rewritten as

$$y_{m,p,k} = \xi_k e^{-j4\pi\frac{\alpha_m\Delta f r_k}{c}} e^{j2\pi f_0\frac{\alpha_m d\sin\theta_k}{c}} e^{j2\pi f_0\frac{\beta_p d\sin\theta_k}{c}}. \tag{11}$$

Since we have P receiving antennas and M matched filter outputs for each receiving antenna, the received signal corresponding to the k-th target can be written in a matrix form as

$$\mathbf{Y}_k = \begin{bmatrix} y_{0,0,k} & y_{0,1,k} & \cdots & y_{0,P-1,k} \\ y_{1,0,k} & y_{1,1,k} & \cdots & y_{1,P-1,k} \\ \vdots & \vdots & \ddots & \vdots \\ y_{M-1,0,k} & y_{M-1,1,k} & \cdots & y_{M-1,P-1,k} \end{bmatrix}. \tag{12}$$

Moreover, defining vectors as

$$\boldsymbol{b}_{\mathrm{t}}(\theta_k) = \left[e^{j2\pi\alpha_0 d\sin(\theta_k)/\lambda}, \cdots, e^{j2\pi\alpha_{M-1} d\sin(\theta_k)/\lambda}\right]^T,$$
$$\boldsymbol{c}_{\mathrm{t}}(r_k) = \left[e^{-j4\pi\alpha_0 \Delta f r_k/c}, \cdots, e^{-j4\pi\alpha_{M-1} \Delta f r_k/c}\right]^T,$$
$$\boldsymbol{a}_{\mathrm{r}}(\theta_k) = \left[e^{j2\pi\beta_0 d\sin(\theta_k)/\lambda}, \cdots, e^{j2\pi\beta_{P-1} d\sin(\theta_k)/\lambda}\right]^T,$$

where $\lambda = c/f_0$ denotes the wavelength of the signal corresponding to f_0, the received signal matrix can be rewritten as

$$\mathbf{Y}_k = \xi_k \left[\boldsymbol{b}_{\mathrm{t}}(\theta_k) \oplus \boldsymbol{c}_{\mathrm{t}}(r_k)\right] \boldsymbol{a}_{\mathrm{r}}^T(\theta_k) \in \mathbb{C}^{M\times P}. \tag{13}$$

So far, we have considered the received signal model only for the k-th target ignoring noise, but actual received signal will be the superposition of the signals from K targets with additive noise. Also, we usually use multiple snapshots for DOA and range estimation, while (13) can be considered as a single snapshot for the k-th target. Thus, the actual sampled received signal model of the l-th snapshot ($l = 0, 1, \cdots, L-1$) including additive noise is written as

$$\mathbf{Y}(l) = \sum_{k=0}^{K-1} \xi_k(l) \left[\boldsymbol{b}_{\mathrm{t}}(\theta_k) \oplus \boldsymbol{c}_{\mathrm{t}}(r_k)\right] \boldsymbol{a}_{\mathrm{r}}^T(\theta_k) + \mathbf{N}(l), \tag{14}$$

where $\mathbf{N}(l) \in \mathbb{C}^{M\times P}$ is a white circular complex Gaussian noise matrix in the l-th snapshot. Using the properties of

$$\mathrm{vec}(\boldsymbol{a}\boldsymbol{b}^T) = \boldsymbol{b} \otimes \boldsymbol{a}, \tag{15}$$

where $\mathrm{vec}(\cdot)$ denotes the vectorization operator, and

$$(\mathbf{A} \oplus \mathbf{C}) \otimes (\mathbf{B} \oplus \mathbf{D}) = (\mathbf{A} \otimes \mathbf{B}) \oplus (\mathbf{C} \otimes \mathbf{D}), \tag{16}$$

the vectorized received signal $\boldsymbol{y}(l) = \mathrm{vec}(\mathbf{Y}(l))$ can be rewritten as [25]

$$\begin{aligned}
\boldsymbol{y}(l) &= \mathrm{vec}(\mathbf{Y}(l)) \\
&= \sum_{k=0}^{K-1} \xi_k(l) \boldsymbol{a}_{\mathrm{r}}(\theta_k) \otimes (\boldsymbol{b}_{\mathrm{t}}(\theta_k) \oplus \boldsymbol{c}_{\mathrm{t}}(r_k)) + \boldsymbol{n}(l) \\
&= \sum_{k=0}^{K-1} \xi_k(l) (\boldsymbol{a}_{\mathrm{r}}(\theta_k) \oplus \mathbf{1}_P) \otimes (\boldsymbol{b}_{\mathrm{t}}(\theta_k) \oplus \boldsymbol{c}_{\mathrm{t}}(r_k)) + \boldsymbol{n}(l) \\
&= \sum_{k=0}^{K-1} \xi_k(l) \left[\mathbf{1}_P \otimes \mathbf{c}_{\mathrm{t}}(r_k)\right] \odot \left[\boldsymbol{a}_{\mathrm{r}}(\theta_k) \otimes \mathbf{b}_{\mathrm{t}}(\theta_k)\right] + \boldsymbol{n}(l)
\end{aligned}$$

$$
\begin{aligned}
&= \sum_{k=0}^{K-1} \xi_k(l)\, \mathrm{diag}\left\{ \left[\mathbf{1}_P \otimes \mathbf{c}_{\mathrm{t}}\left(r_k\right)\right] \left[\boldsymbol{a}_{\mathrm{r}}\left(\theta_k\right) \otimes \mathbf{b}_{\mathrm{t}}\left(\theta_k\right)\right]^T \right\} + \boldsymbol{n}(l) \\
&= \sum_{k=0}^{K-1} \xi_k(l)\, \mathrm{diag}\left\{ \mathbf{1}_P \otimes \left[\mathbf{c}_{\mathrm{t}}\left(r_k\right) \left[\boldsymbol{a}_{\mathrm{r}}\left(\theta_k\right) \otimes \mathbf{b}_{\mathrm{t}}\left(\theta_k\right)\right]^T \right] \right\} + \boldsymbol{n}(l) \\
&= \mathrm{diag}\left(\sum_{k=0}^{K-1} \xi_k(l) \mathbf{1}_P \otimes \left[\mathbf{c}_{\mathrm{t}}\left(r_k\right) \left(\boldsymbol{a}_{\mathrm{r}}\left(\theta_k\right) \otimes \boldsymbol{b}_{\mathrm{t}}\left(\theta_k\right)\right)^T \right] \right) + \boldsymbol{n}(l), \qquad (17)
\end{aligned}
$$

where

$$
\boldsymbol{n}(l) = \mathrm{vec}(\mathbf{N}(l)). \qquad (18)
$$

Note that the conventional FDA MIMO radar in [19] has employed a ULA for the physical array, and the entire ULA is used both for the transmitting and the receiving arrays, hence $\Phi = \Phi_{\mathrm{t}} = \Phi_{\mathrm{r}}$ holds. On the other hand, in [25], a ULA is also employed for the physical array and the entire ULA is used for the transmitting array, but a sparse array, which is composed by the subarray of the ULA, is used for the receiving array to reduce the computational complexity. Thus, $\Phi = \Phi_{\mathrm{t}} \supseteq \Phi_{\mathrm{r}}$ holds in this case.

3 Proposed Design of Nested FDA for MIMO Radar

Here, we consider to introduce the sparse array into the physical array of the FDA MIMO radar to improve the estimation performance. Since the selection of the sparse array configuration will have large impact on the performance, an appropriate choice of the sparse array for the FDA MIMO radar will be required.

Our method is based on [19] and we also utilize the 2D ANM based joint DOA and range estimation approach. As we'll see in Section 5, the transmitting array is required to have the ULA structure in order to solve the 2D ANM problem by reducing it to SDP problem taking advantage of Vandermonde decomposition of multilevel Toeplitz matrix. This means that the physical sparse array for the FDA MIMO radar should have ULA structure in its subarray. Thus, we have employed nested array [16] for the physical sparse array, as it has an inner ULA as a subarray.

The location set Φ of the nested array is defined with location sets of two uniform linear subarrays

$$
\Phi_1 = \{k_1 d, 0 \le k_1 \le M-1, k_1 \in \mathbb{N}\}, \qquad (19)
$$

$$
\Phi_2 = \{(Mk_2 - 1)d, 2 \le k_2 \le N-M+1, k_2 \in \mathbb{N}\}, \qquad (20)
$$

as $\Phi = \Phi_1 \cup \Phi_2$. In the proposed approach, we use the inner ULA defined by (19) as the transmitting array, namely, $\Phi_{\mathrm{t}} = \Phi_1$. On the other hand, we use whole nested array as the receiving array, that is $\Phi_{\mathrm{r}} = \Phi$. Figure 2 illustrates the structure of the proposed nested FDA for the co-located MIMO radar.

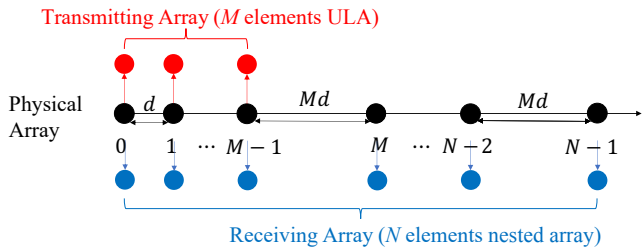

Figure 2: Proposed nested FDA for co-located MIMO radar.

In the received signal model of (17), DOA information is included in $\boldsymbol{a}_{\mathrm{r}}(\theta_k) \otimes \boldsymbol{b}_{\mathrm{t}}(\theta_k)$, whose virtual array aperture A is given by

$$A = NM - M^2 + 2M - 2. \tag{21}$$

Therefore, the DOA estimation performance could be improved by the design to maximize the aperture. On the other hand, in (17), $\boldsymbol{c}_{\mathrm{t}}(r_k)$ contains the range information, whose dimension is equal to the number of transmitting antenna elements M. Thus, from a viewpoint of the range estimation performance, better estimation results could be expected with larger M. This means that both the virtual array aperture A and the number of transmitting antenna elements M should be taken into consideration in the design of the proposed nested FDA for the MIMO radar.

We have noticed that the level of the nested array, which is defined as $F = N - M$, can be used to control the aperture and the number of elements of the transmitting array, because, for given N, a selection of the level F uniquely determines A and M. Table 1 shows examples of the pairs of A and M for ULA FDA [19] and different levels of the nested FDA with the number of physical elements $N = 6, 8$, and 10, respectively. From the table, we can see that the maximum virtual array aperture A is not necessarily achieved with the largest number of transmitting antenna elements M. Thus, the level of the proposed nested FDA should be determined by the compromise between DOA and range estimation performance.

Table 1: Examples of virtual array aperture A and number of transmitting antenna elements M of ULA FDA [19] and proposed nested FDA.

Array Structure	$N = 6$	$N = 8$	$N = 10$
ULA FDA	A=10, M=6	A=14, M=8	A=18, M=10
1-level nested FDA	A=13, M=5	A=19, M=7	A=25, M=9
2-level nested FDA	A=14, M=4	A=22, M=6	A=30, M=8
3-level nested FDA	A=13, M=3	A=23, M=5	A=33, M=7

4 DOA-range Decoupling for Proposed Nested FDA MIMO Radar

In order to avoid the ambiguity in the estimation, the received signal model with decoupled DOA and range information will be discussed here.

If we divide the received signal vector $\boldsymbol{y}(l)$ into N subvectors of size $M \times 1$ as

$$\boldsymbol{y}(l) = [\boldsymbol{y}_0^T(l), \cdots, \boldsymbol{y}_{N-1}^T(l)]^T, \tag{22}$$

the n-th subvector can be written as

$$\boldsymbol{y}_n(l) = \text{diag}\left(\sum_{k=0}^{K-1} \xi_k(l)\boldsymbol{c}_\text{t}(r_k)\,\boldsymbol{b}_\text{t}^T(\theta_k)\,a_\text{r}^n(\theta_k)\right) + \boldsymbol{n}_n(l), \tag{23}$$

where $a_\text{r}^n(\theta_k)$ denotes the n-th element of $\boldsymbol{a}_\text{r}(\theta_k)$.

We define a steering vector with respect to θ_k as

$$\boldsymbol{g}(\theta_k) = \left[1, e^{j2\pi d\sin(\theta_k)/\lambda}, \cdots, e^{j2\pi(M-1+\beta_{N-1})d\sin(\theta_k)/\lambda}\right]^T \in \mathbb{C}^{(M+\beta_{N-1})\times 1}, \tag{24}$$

which contains all elements in $\mathbf{a}_\text{r}(\theta_k) \otimes \mathbf{b}_\text{t}(\theta_k)$ but without duplication, where $\beta_{N-1} = (N-M+1)M-1$ for the case with the nested array. Then, using the operator of $\text{diag}_k(\mathbf{D})$, (23) can be simplified as

$$\begin{aligned}\boldsymbol{y}_n(l) &= \text{diag}_{\beta_n}\left(\sum_{k=0}^{K-1} \xi_k(l)\boldsymbol{c}_\text{t}(r_k)\,\boldsymbol{g}^T(\theta_k)\right) + \boldsymbol{n}_n(l) \\ &= \mathbf{Q}_n \sum_{k=0}^{K-1} \xi_k(l)\left(\boldsymbol{g}(\theta_k) \otimes \boldsymbol{c}_\text{t}(r_k)\right) + \boldsymbol{n}_n(l),\end{aligned} \tag{25}$$

where $\mathbf{Q}_n \in \mathbb{C}^{M\times M(M+\beta_{N-1})}$ is the extraction matrix, whose element is one at the $\{1+\beta_n M+(M+1)m\}$-th column of the m-th row ($m=0,1,\ldots,M-1, n=0,1,\ldots,N-1$) and zero otherwise, and $\boldsymbol{n}(l)=[\boldsymbol{n}_0^T(l),\cdots,\boldsymbol{n}_{N-1}^T(l)]^T$. Note that the definition of the extraction matrix $\mathbf{Q}_n$ in this paper is different from that in [19] or [25]. In order to help an intuitive understanding, Table 2 visually shows the configuration of the extraction matrix $\mathbf{Q}_n$, where each cell contains a row vector of size M and $\boldsymbol{e}_M^k$ represents a $1\times M$ vector with all-zero except that the k-th element is 1. Note that the index of the column in Table 2, such as β_n and $1+\beta_n$, corresponds to the block index of the matrix $\mathbf{Q}_n$.

Table 2: Configuration of extraction matrix $\mathbf{Q}_n$.

index	1	$\cdots$	β_n	$1+\beta_n$	$2+\beta_n$	$\cdots$	$M-1+\beta_n$	$M+\beta_n$	$M+\beta_n+1$	$\cdots$	$M+\beta_{N-1}$
0	$\mathbf{0}_M^T$	$\cdots$	$\mathbf{0}_M^T$	$\boldsymbol{e}_M^1$	$\mathbf{0}_M^T$	$\cdots$	$\mathbf{0}_M^T$	$\mathbf{0}_M^T$	$\mathbf{0}_M^T$	$\cdots$	$\mathbf{0}_M^T$
1	$\mathbf{0}_M^T$	$\cdots$	$\mathbf{0}_M^T$	$\mathbf{0}_M^T$	$\boldsymbol{e}_M^2$	$\cdots$	$\mathbf{0}_M^T$	$\mathbf{0}_M^T$	$\mathbf{0}_M^T$	$\cdots$	$\mathbf{0}_M^T$
$\vdots$	$\vdots$		$\vdots$	$\vdots$	$\vdots$	$\ddots$	$\vdots$	$\vdots$	$\vdots$		$\vdots$
$M-2$	$\mathbf{0}_M^T$	$\cdots$	$\mathbf{0}_M^T$	$\mathbf{0}_M^T$	$\mathbf{0}_M^T$	$\cdots$	$\boldsymbol{e}_M^{M-1}$	$\mathbf{0}_M^T$	$\mathbf{0}_M^T$	$\cdots$	$\mathbf{0}_M^T$
$M-1$	$\mathbf{0}_M^T$	$\cdots$	$\mathbf{0}_M^T$	$\mathbf{0}_M^T$	$\mathbf{0}_M^T$	$\cdots$	$\mathbf{0}_M^T$	$\boldsymbol{e}_M^M$	$\mathbf{0}_M^T$	$\cdots$	$\mathbf{0}_M^T$

By stacking both sides of (25), we have

$$\boldsymbol{y}(l)=\mathbf{Q}\left[\mathbf{G}(\boldsymbol{\theta})\odot\mathbf{C}_{\mathrm{t}}(\boldsymbol{r})\right]\boldsymbol{\xi}(t)+\boldsymbol{n}(l), \tag{26}$$

where

$$\mathbf{Q}=\left[\mathbf{Q}_0^T,\cdots,\mathbf{Q}_{N-1}^T\right]^T, \tag{27}$$
$$\mathbf{G}(\boldsymbol{\theta})=\left[\boldsymbol{g}\left(\theta_0\right),\cdots,\boldsymbol{g}\left(\theta_{K-1}\right)\right], \tag{28}$$
$$\mathbf{C}_{\mathrm{t}}(\boldsymbol{r})=\left[\boldsymbol{c}_{\mathrm{t}}\left(r_0\right),\cdots,\boldsymbol{c}_{\mathrm{t}}\left(r_{K-1}\right)\right], \tag{29}$$
$$\boldsymbol{\xi}(l)=\left[\xi_0(l),\cdots,\xi_{K-1}(l)\right]^T. \tag{30}$$

Moreover, the received signal matrix composed by L snapshots is given by

$$\bar{\mathbf{Y}}=\mathbf{Q}\left[\mathbf{G}(\boldsymbol{\theta})\odot\mathbf{C}_{\mathrm{t}}(\boldsymbol{r})\right]\boldsymbol{\xi}+\mathbf{N}\in\mathbb{C}^{MN\times L}, \tag{31}$$

where

$$\bar{\mathbf{Y}}=\left[\boldsymbol{y}(0),\cdots,\boldsymbol{y}(L-1)\right], \tag{32}$$
$$\boldsymbol{\xi}=\left[\boldsymbol{\xi}(0),\cdots,\boldsymbol{\xi}(L-1)\right], \tag{33}$$
$$\mathbf{N}=\left[\boldsymbol{n}(0),\cdots,\boldsymbol{n}(L-1)\right]. \tag{34}$$

Note that $\mathbf{G}(\boldsymbol{\theta})$ depends only on the DOA information of $\boldsymbol{\theta}=[\theta_0,\cdots,\theta_{K-1}]^T$ and $\mathbf{C}_{\mathrm{t}}(\boldsymbol{r})$ depends only on the range information of $\boldsymbol{r}=[r_0,\cdots,r_{K-1}]^T$, thus the DOA-range decoupling has been achieved in (31) with the manipulations above.

5 DOA and Range Estimation Method

To fully utilize the extended virtual array aperture of the proposed nested FDA and reduce required number of snapshots, we employ the 2D ANM approach as in [19].

From (31), we can regard the available received signal matrix $\bar{\mathbf{Y}}$ as the result of the extraction by using $\mathbf{Q}$ from an ideal received signal matrix of

$$\hat{\mathbf{Y}} = \mathbf{G}(\boldsymbol{\theta}) \odot \mathbf{C}_{\mathrm{t}}(\boldsymbol{r})\boldsymbol{\xi} \tag{35}$$

and the addition of the noise matrix. Thus, we firstly consider the ANM for the received signal model of (35) for simplicity.

According to [28],[29], the solution of ANM for (35) is obtained by solving a SDP problem with variables $\mathbf{V}$ and $\boldsymbol{u}$ as

$$\begin{aligned} &\min_{\boldsymbol{u},\mathbf{V}} \frac{1}{2\sqrt{MN}}[\mathrm{tr}(\mathbf{T}(\boldsymbol{u})) + \mathrm{tr}(\mathbf{V})] \\ &\text{s.t} \begin{bmatrix} \mathbf{T}(\boldsymbol{u}) & \hat{\mathbf{Y}} \\ \hat{\mathbf{Y}}^H & \mathbf{V} \end{bmatrix} \succeq 0, \end{aligned} \tag{36}$$

where $\boldsymbol{u}$ is given by

$$\begin{aligned} \boldsymbol{u} =& [u_{0,0}, u_{0,1}, \cdots, u_{0,N-1}, u_{1,-(N-1)}, u_{1,-(N-2)}, \cdots, u_{1,N-1}, \cdots, \\ & u_{M-1,-(N-1)}, u_{M-1,-(N-2)}, \cdots, u_{M-1,-N-1}]^T \in \mathbb{C}^{[(M-1)(2N-1)+N]\times 1}. \end{aligned}$$

$\mathbf{T}(\boldsymbol{u})$ is defined as a mapping from a vector $\boldsymbol{u}$ to an $MN \times MN$ matrix with $M \times M$ blocks as

$$\mathbf{T}(\boldsymbol{u}) = \begin{bmatrix} \mathbf{T}_0 & \mathbf{T}_1^H & \cdots & \mathbf{T}_{M-1}^H \\ \mathbf{T}_1 & \mathbf{T}_0 & \cdots & \mathbf{T}_{M-2}^H \\ \vdots & \vdots & \ddots & \vdots \\ \mathbf{T}_{M-1} & \mathbf{T}_{M-2} & \cdots & \mathbf{T}_0 \end{bmatrix},$$

where each block of $\mathbf{T}(\boldsymbol{u})$ is an $N \times N$ Toeplitz matrix expressed as

$$\mathbf{T}_m = \begin{bmatrix} u_{m,0} & u_{m,-1} & \cdots & u_{m,-(N-1)} \\ u_{m,1} & u_{m,0} & \cdots & u_{m,-(N-2)} \\ \vdots & \vdots & \ddots & \vdots \\ u_{m,N-1} & u_{m,N-2} & \cdots & u_{m,0} \end{bmatrix}, m = 0, 1, \cdots, M-1.$$

Moreover, $\mathbf{T}(\boldsymbol{u})$ can be written as the Vandermonde decomposition form as

$$\mathbf{T}(\boldsymbol{u}) = (\mathbf{G}(\boldsymbol{\theta}) \odot \mathbf{C}_{\mathrm{t}}(\boldsymbol{r}))\, \boldsymbol{\Gamma}\, (\mathbf{G}(\boldsymbol{\theta}) \odot \mathbf{C}_{\mathrm{t}}(\boldsymbol{r}))^H, \tag{37}$$

where $\mathbf{\Gamma} = \text{diag}\,(\sigma_0, \cdots, \sigma_{K-1})$ denotes a diagonal matrix whose diagonal elements are the eigenvalues of $\mathbf{T}(\boldsymbol{u})$.

In order to solve (36) as the SDP problem, $\mathbf{T}(\boldsymbol{u})$ must be a twofold block Toeplitz (2-level Toeplitz) matrix. According to the property of the Vandermonde decomposition, $\mathbf{C}_{\text{t}}(\boldsymbol{r})$ must be a Vandermonde matrix to satisfy the requirement (see Appendix A.2). This means that the transmitting array is required to be a ULA in order to solve the ANM as the SDP problem. This is the reason why we have selected nested array and utilized its inner ULA for the transmitting array in Section 3.

Since the ideal received signal matrix $\hat{\mathbf{Y}}$ is not available, we need to use the received signal model of

$$\bar{\mathbf{Y}} = \mathbf{Q}\hat{\mathbf{Y}} + \mathbf{N}. \tag{38}$$

Thus, taking the extraction matrix $\mathbf{Q}$ and the additive noise into consideration, we solve the regularized version of (36) given by

$$\begin{aligned} \min_{\boldsymbol{u},\mathbf{V},\hat{\mathbf{Y}}} \frac{1}{2\sqrt{MN}}[\text{tr}(\mathbf{T}(\boldsymbol{u})) + \text{tr}(\mathbf{V})] + \frac{\mu}{2}\|\bar{\mathbf{Y}} - \mathbf{Q}\hat{\mathbf{Y}}\|_F \\ \text{s.t} \begin{bmatrix} \mathbf{T}(\boldsymbol{u}) & \hat{\mathbf{Y}} \\ \hat{\mathbf{Y}}^H & \mathbf{V} \end{bmatrix} \succeq 0, \end{aligned} \tag{39}$$

where $\mu \geq 0$ is a regularization parameter. Algorithm 1 shows the specific process to solve the SDP problem in (39) with CVX toolbox. Once the estimate of $\mathbf{T}(\boldsymbol{u})$ are obtained with Algorithm 1, we utilize the idea of the 2D ESPRIT algorithm [22] to obtain grid-free DOA and range estimates from $\mathbf{T}(\boldsymbol{u})$, since it corresponds to the correlation matrix of the ideal received signal matrix whose array manifold is $\mathbf{G}(\boldsymbol{\theta}) \odot \mathbf{C}_{\text{t}}(\boldsymbol{r})$, while the MUSIC based algorithm has been used in [19].

6 Computational Complexity

To evaluate the computational cost of the proposed 2D ANM algorithm, we provide a theoretical complexity analysis of the algorithm and compare it with the complexities of several existing algorithms, including the MUSIC based algorithm [8], GFT based algorithm [23], and hybrid algorithm [9], which will be used for performance comparison in Section 7. Table 3 summarizes the computational complexity of each method using big-O notation. In the table, η_1 and η_2 represent the number of searches for 2D parameters θ and r, respectively, in the MUSIC based algorithm and the GFT based algorithm, while b denotes the number of iterations required in the hybrid algorithm to converge.

Algorithm 1 2D ANM algorithm for FDA MIMO radar.

Input: Received signal matrix $\bar{\mathbf{Y}}$, regularization parameter μ, stacked extraction matrix $\mathbf{Q}$;

Output: Equivalent correlation matrix $\mathbf{T}(\boldsymbol{u})$;

1: Construct SDP minimization problem in (39);

2: Randomly initialize $\mathbf{V}$, $\mathbf{T}(\boldsymbol{u})$, and $\hat{\mathbf{Y}}$ under the constraints and construct the initial semi-positive defined matrix

$$\begin{bmatrix} \mathbf{T}(\boldsymbol{u}) & \hat{\mathbf{Y}} \\ \hat{\mathbf{Y}}^H & \mathbf{V} \end{bmatrix} \succeq 0;$$

3: Solve the SDP problem by CVX toolbox;

4: **return** $\mathbf{T}(\boldsymbol{u})$;

Table 3: Computational complexity of the algorithms.

Algorithms	Computational complexity
2D ANM	$O([M(MN-M^2+2M-1)+L]^{4.5})$
MUSIC based	$O(4/3(MN)^3+(K+\eta_1+\eta_2)L(MN)^2)$ [8]
GFT based	$O(\eta_1\eta_2(MN)^3+\eta_1\eta_2L(MN)^2)$
Hybrid	$O(b(MN)^3+bLK(MN)^2+bK(L+1)MN)$ [9]

We can see from the table that the 2D ANM algorithm has the highest complexity, due to the high computation burden in solving the SDP problem [14]. The complexities of the MUSIC based, GFT based, and hybrid algorithms scale cubically with respect to MN, but their actual computational costs differ due to different constant factors. The MUSIC based algorithm has a relatively small constant of 4/3, while the constants of the GFT based and hybrid algorithms depend on the numbers of 2D search points and iterations, which are typically large in practice. Consequently, the actual computational costs of the GFT based and hybrid algorithms are often higher than that of the MUSIC based algorithm.

7 Simulation Results

To confirm the validity of the proposed approach, we have evaluated root-mean-square error (RMSE) performance of the proposed nested FDA MIMO radar using the 2D ANM via computer simulations. Operating frequency at the 0-th element f_0 and the unit frequency shift of the FDA Δf are set to be 10GHz and 5kHz, respectively. Based on the settings in [19] and [25], three

targets are assumed with DOA and range pairs of $(\theta_0, r_0) = (10°, 4000\text{m})$, $(\theta_1, r_1) = (20°, 12000\text{m})$, and $(\theta_2, r_2) = (40°, 6000\text{m})$ except for the simulation results under closely spaced targets in Figure 3.

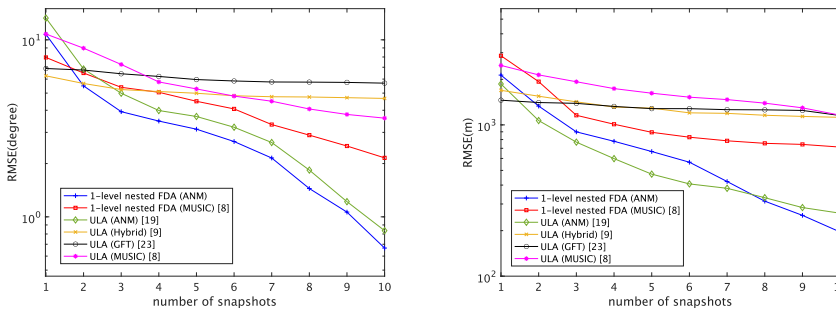

(a) DOA estimation. (b) Range estimation.

Figure 3: RMSE versus number of snapshots with closely spaced targets ($N = 10$).

In order to compare the performance obtained via simulations with theoretical performance bound, we have derived CRLBs [12] for each antenna configuration. Define η_{θ_k} and η_{r_k} as the CRLBs of DOA and range estimates for the k-th target, and

$$\boldsymbol{a}\left(\theta_k, r_k\right) = \left[\boldsymbol{b}_{\mathrm{t}}\left(\theta_k\right) \oplus \boldsymbol{c}_{\mathrm{t}}\left(r_k\right)\right] \otimes \boldsymbol{a}_{\mathrm{r}}\left(\theta_k\right), \tag{40}$$

$$\mathbf{A}\left(\boldsymbol{\theta}, \boldsymbol{r}\right) = \left[\boldsymbol{a}\left(\theta_0, r_0\right), \ldots, \boldsymbol{a}\left(\theta_{K-1}, r_{K-1}\right)\right], \tag{41}$$

CRLB vector $\boldsymbol{\eta} = [\eta_{\theta_0}, \cdots, \eta_{\theta_{K-1}}, \eta_{r_0}, \cdots, \eta_{r_{K-1}}]^T$ is obtained as

$$\boldsymbol{\eta} = \operatorname{diag}\left(\frac{\sigma^2}{2L} \operatorname{Re}\left\{\left(\mathbf{W}^H \boldsymbol{\Pi}_{\mathbf{A}}^{\perp} \mathbf{W}\right) \odot \mathbf{P}^T\right\}^{-1}\right), \tag{42}$$

where σ^2 denotes the noise variance, and

$$\mathbf{W} = \left[\mathbf{A}_\theta, \mathbf{A}_r\right] = \left[\frac{\partial \mathbf{A}\left(\boldsymbol{\theta}, \boldsymbol{r}\right)}{\partial \boldsymbol{\theta}}, \frac{\partial \mathbf{A}\left(\boldsymbol{\theta}, \boldsymbol{r}\right)}{\partial \boldsymbol{r}}\right], \tag{43}$$

$$\boldsymbol{\Pi}_{\mathbf{A}}^{\perp} = \mathbf{I} - \mathbf{A}\left(\boldsymbol{\theta}, \boldsymbol{r}\right)\left(\mathbf{A}\left(\boldsymbol{\theta}, \boldsymbol{r}\right)^H \mathbf{A}\left(\boldsymbol{\theta}, \boldsymbol{r}\right)\right)^{-1} \mathbf{A}\left(\boldsymbol{\theta}, \boldsymbol{r}\right)^H. \tag{44}$$

Moreover, $\mathbf{P}$ is a block matrix defined as

$$\mathbf{P} = \begin{bmatrix} \mathbf{P}_0 & \mathbf{P}_0 \\ \mathbf{P}_0 & \mathbf{P}_0 \end{bmatrix}, \tag{45}$$

where

$$\mathbf{P}_0 = \mathbf{R}_\xi \mathbf{A}\left(\boldsymbol{\theta}, \boldsymbol{r}\right)^H \mathbf{R}_{\bar{\mathbf{Y}}}^{-1} \mathbf{A}\left(\boldsymbol{\theta}, \boldsymbol{r}\right) \mathbf{R}_\xi, \tag{46}$$

$\mathbf{R}_{\bar{\mathbf{Y}}} = E[\bar{\mathbf{Y}}\bar{\mathbf{Y}}^H]/L$ is the covariance matrix of received signal, and $\mathbf{R}_\xi = E[\boldsymbol{\xi}\boldsymbol{\xi}^H]/L$.

Figure 4 shows the estimation results of 100 simulation trials with 100 points for each target using the proposed 1-level nested FDA MIMO radar with the number of physical antennas $N = 8$, the number of snapshots $L = 10$, and the received signal-to-noise ratio (SNR) of 10 dB. From Figure 4, we can see that the DOAs and ranges of all 3 targets are estimated with high accuracy without large deviation in spite of such a small number of snapshots.

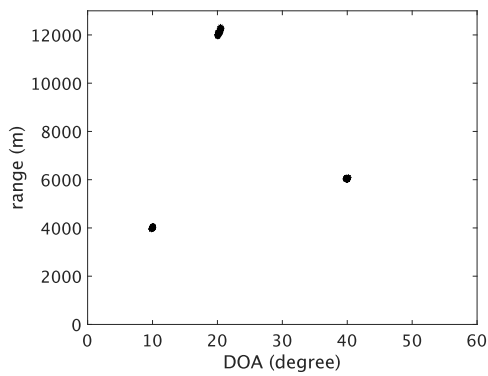

Figure 4: Scatter plots of estimated DOAs and ranges for 100 simulation trials.

Figures 5a and 5b respectively depict the RMSE performance of the DOA and range estimation versus the number of snapshots for the 1-level nested FDA using the proposed 2D ANM algorithm, the MUSIC based algorithm [8], the 2D ANM algorithm in [19], the GFT based algorithm [23], and the hybrid algorithm in [9] with SNR of 10 dB and the number of antenna elements of $N = 10$. Note that, except for the proposed 2D ANM algorithm and the MUSIC based algorithm, the array structure is assumed to be the ULA due to the limitations of the algorithms. The search steps of the DOA and range are set to be 0.1° and 50m, respectively for the method in [8], while the grids of the overcomplete dictionary are set to 1° and 50m for the methods in [23] and [9], to balance computational complexity among different methods. The RMSE for each number of snapshots is obtained by the average of 200 simulation trials. From the DOA estimation performance results in Figure 5a, it can be seen that when the number of snapshots is small, the performance of the GFT based and hybrid algorithms based on CS is better than the

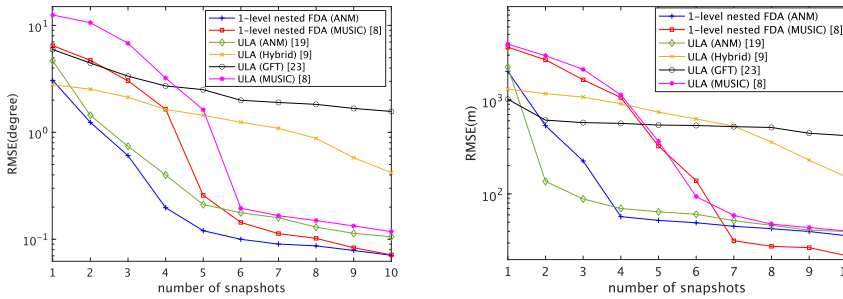

(a) DOA estimation. (b) Range estimation.

Figure 5: RMSE versus number of snapshots ($N = 10$).

MUSIC based algorithm. The proposed 1-level nested FDA achieves even better RMSE performance than the state-of-the-art methods, especially for the small number of snapshots region except when the number of snapshots is 1. On the other hand, from the range estimation results in Figure 5b, it can be found that the GFT based and the hybrid algorithms still have outstanding performance when the number of snapshots is small, while the proposed 1-level nested FDA (ANM) achieves better performance in this region except for the case with the number of snapshots of 1. Moreover, the proposed 1-level nested FDA achieves better RMSE performance than that of the ANM algorithm using the ULA for the number of snapshots greater than or equal to 4, thanks to the improved DOA estimates due to the expanded array aperture.

To further evaluate the robustness and practical performance of the proposed 2D ANM algorithm under more realistic and challenging conditions, we conduct a new simulation experiment involving closely spaced targets. In this scenario, two targets are intentionally placed in close proximity in both DOA and range dimensions as $(\theta_0, r_0) = (10°, 4000\text{m})$, $(\theta_1, r_1) = (12°, 4500\text{m})$, while a third target is positioned far from them at $(\theta_2, r_2) = (40°, 8000\text{m})$. Figures 3a and 3b present the DOA and range estimation RMSEs versus the number of snapshots under this scenario with all other parameters identical to those in Figures 5a and 5b. It is observed that the proposed 2D ANM algorithm applied to the nested FDA configuration maintains high estimation accuracy even when targets are closely spaced. Specifically, the proposed method outperforms the other techniques in DOA estimation for all but the single-snapshot case, and shows competitive performance in range estimation. These results demonstrate the strong resolution capability and robustness of our approach in difficult operating conditions.

Figures 6 and 7 present the RMSE performance of the proposed nested FDA MIMO radar with different levels of the nested array using the 2D ANM

for the DOA and the range estimation, respectively, versus the received SNR with $N = 6$ and $L = 10$. To facilitate comparison, the performance of the existing FDA MIMO radar using ULA FDA [19] with $M = N = 6$ and CRLB for each array configuration are also plotted in the figures. The RMSE for each SNR is obtained by the average of 200 simulation trials. From Figure 6, it can be observed that the DOA estimation performance of the proposed nested FDA is better than that of ULA FDA regardless of the level of the nested array. Among the three proposed nested FDAs, 2-level nested FDA achieves the best performance. This would be because 2-level nested FDA has a larger virtual array aperture of $A = 14$ than that of 1 or 3-level nested FDA of $A = 13$ as discussed in Section 3. On the other hand, from Figure 7, we can see that the ULA FDA achieves the best range estimation performance. Moreover, the proposed nested FDA achieves better performance for lower levels of the nested array. This is because, for a given number of physical antenna elements, the ULA FDA utilizes the largest number of elements for the signal transmission among the four methods, and the number of transmitting antennas decreases as the level of the nested array increases. These numerical results demonstrate that the proposed nested FDA can control the balance between DOA and range estimation performance by adjusting the level of the nested array. In practical applications, an appropriate level of the nested array should be selected depending on the requirement on the DOA and range estimation performance.

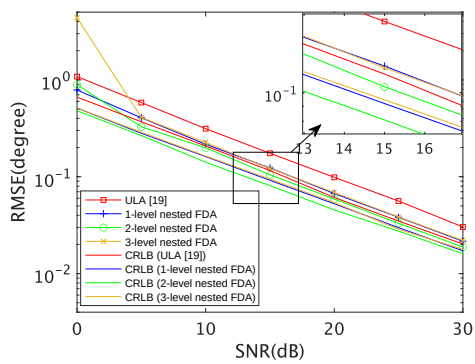

Figure 6: RMSE of DOA estimation versus received SNR of different array configurations ($N = 6$).

Figures 8 and 9 also illustrate the DOA and range RMSE performance for the same system setting as in Figures 6 and 7 but with a larger number of physical antenna elements of $N = 10$. As seen from Figure 8, the proposed 3-level nested FDA achieves the best DOA estimation performance, since it has the greatest virtual array aperture, which again supports the discussions in

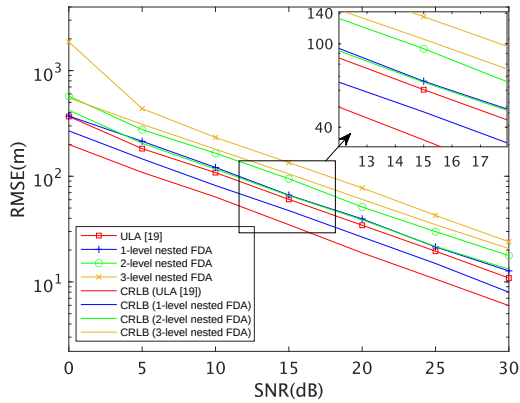

Figure 7: RMSE of range estimation versus received SNR of different array configurations ($N = 6$).

Section 3. Moreover, the proposed 2 or 3-level nested FDA achieves the RMSE performance very close to their CRLBs. On the other hand, the range estimation performance largely depends on the number of transmitting antennas again, and thus the proposed nested FDA with a lower level of the nested array achieves better range performance. However, it should be noted here that, unlike the case in Figure 7, the proposed 1 or 2-level nested FDA can achieve better RMSE performance than that of the ULA FDA, which has the largest number of transmitting antennas. This could be attributed to the fact that the range estimation accuracy also depends on the estimation accuracy of DOA, so the degradation due to smaller number of transmitted antennas is compensated by the improved DOA estimation accuracy due to the larger virtual array aperture for the case with 1 or 2-level nested FDA. This phenomenon does not appear in simulations in Figure 7 with $N = 6$, where the impact of decreasing transmitting antenna is relatively larger than the case with $N = 10$. The results here suggest that the proposed approach using the nested FDA will be more effective for the MIMO radar with larger number of antennas.

In practical radar systems, mutual coupling (MC) among antenna elements can significantly distort the array manifold, leading to degraded estimation performance. While the signal model in Section 2 assumes an MC-free situation, we now evaluate the performance of the proposed nested FDA MIMO scheme under realistic MC conditions.

To this end, we adopt a widely used MC model [10, 11, 13], and the received signal with the MC effect is expressed as

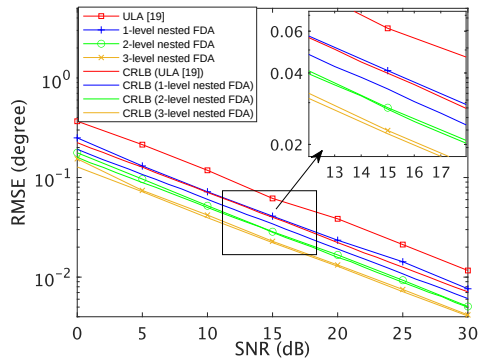

Figure 8: RMSE of DOA estimation versus received SNR of different array configurations ($N = 10$).

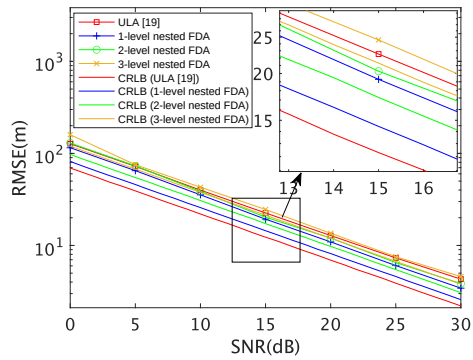

Figure 9: RMSE of range estimation versus received SNR of different array configurations ($N = 10$).

$$\mathbf{Y}(l) = \sum_{k=0}^{K-1} \xi_k(l)\mathbf{C}_{\mathrm{t}} \left[\boldsymbol{b}_{\mathrm{t}}\left(\theta_k\right) \oplus \boldsymbol{c}_{\mathrm{t}}\left(r_k\right)\right] \boldsymbol{a}_{\mathrm{r}}^{T}\left(\theta_k\right) \mathbf{C}_{\mathrm{r}}^{T} + \mathbf{N}(l), \tag{47}$$

where the MC effect is represented by matrices $\mathbf{C}_{\mathrm{t}} \in \mathbb{C}^{M\times M}$ and $\mathbf{C}_{\mathrm{r}} \in \mathbb{C}^{P\times P}$ applied to the transmitting and receiving arrays, respectively. The (i, j)-th element of $\mathbf{C}_{\mathrm{t}}$ is defined as

$$\mathbf{C}_{\mathrm{t}}(i,j) = \begin{cases} 0, & |\alpha_i - \alpha_j| > B \\ c_{|\alpha_i-\alpha_j|}, & |\alpha_i - \alpha_j| \le B \end{cases},$$

where $c_0 = 1$, c_1 is the MC coefficient between antenna pairs with unit spacing d, $c_n = c_1 e^{-j(n-1)\pi/8}/n, (2 \le n \le B)$, and B denotes the maximum distance with the MC effect. Similarly, the (p, q)-th element of $\mathbf{C}_\mathrm{r}$ can be defined as

$$\mathbf{C}_\mathrm{r}(p,q) = \begin{cases} 0, & |\beta_p - \beta_q| > B \\ c_{|\beta_p - \beta_q|}, & |\beta_p - \beta_q| \le B \end{cases}.$$

To assess the impact of MC on estimation performance, we have conducted simulations to evaluate DOA and range RMSEs with and without the MC effect, whose results are shown in Figure 10. ULA and 1-level nested FDA are used for comparison with the physical antenna elements $N = 10$, and the number of snapshots $L = 10$. In the presence of MC, we set $c_1 = 0.1$ and $B = 10$. It is observed that while both systems experience some degradation, the nested FDA maintains superior robustness and estimation accuracy, particularly at moderate-to-high SNR.

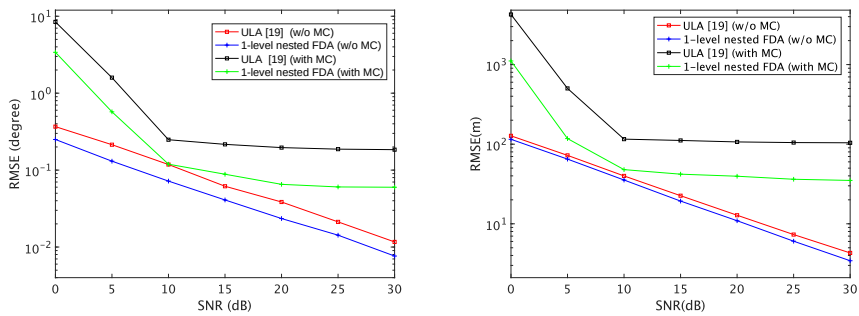

(a) DOA estimation. (b) Range estimation.

Figure 10: RMSE versus received SNR with and without MC effect ($N = 10$).

Meanwhile, to quantify the impact of MC, we introduce the coupling leakage ρ to measure the strength of the MC effect for an array, defined as [10]

$$\rho = \frac{\|\mathbf{C} - \mathbf{I}\|_F}{\|\mathbf{C}\|_F}, \tag{48}$$

where $\mathbf{C}$ represents the MC matrix and $\mathbf{I}$ denotes the identity matrix. Table 4 compares the coupling leakage ρ for different array configurations with $c_1 = 0.1$ and $B = 10$. The results show that nested arrays exhibit leakages consistently lower than that of the ULA structure, especially as the nesting level increases. This implies that nested arrays are inherently more robust to coupling effects due to their sparse structures.

In practical radar applications, some targets may be highly correlated or even completely coherent, severely degrading the performance of traditional

Table 4: Coupling leakage ρ of ULA and nested arrays.

Array Structure	$N = 6$	$N = 8$	$N = 10$
ULA	0.1456	0.1523	0.1566
1-level nested array	0.1299	0.1404	0.1471
2-level nested array	0.1127	0.1275	0.1369
3-level nested array	0.0962	0.1138	0.1262

subspace-based estimation methods because they rely on the full-rank condition of the signal covariance matrix. Figure 11 shows the DOA and range RMSE performance of the 2D ANM algorithm and the MUSIC based algorithm [8] for ULA FDA and 1-level nested FDA, as well as the GFT based algorithm [23] and the hybrid algorithm [9] with ULA, where the two of the three targets are completely coherent, the received SNR is 10 dB, and the number of physical antennas is $N = 10$. It can be seen from the figure that the 2D ANM algorithm achieves consistently accurate DOA and range estimation, while the MUSIC based algorithm suffers from considerable performance degradation compared with the non-coherent scenario in Figure 5 due to the rank deficiency of the covariance matrix. The reason for the good performance of the 2D ANM algorithm could be attributed to the fact that it does not rely on subspace decomposition of the sample covariance matrix. Instead, the 2D ANM algorithm utilizes an optimization framework, where a structured covariance-like matrix (i.e. $\mathbf{T}(\boldsymbol{u})$) is iteratively constructed as an optimization variable under the constraint of positive semi-definiteness. This optimization process would bypass the rank-deficiency issue, which can be observed in conventional subspace methods, allowing the matrix to maintain full rank even when the input signals are coherent.

In order to demonstrate the controllability of the balance between DOA and range estimation performance with the proposed approach, we provide the DOA and the range RMSE of the proposed nested FDA MIMO radar for the number of physical antennas 10 in Figure 12, with SNR of 20 dB and the number of snapshots of $L = 10$. For comparison purpose, the performance of ULA FDA [19] is also plotted in the figure. Note that the results for the higher levels of nested array with reduced array aperture are not shown in the figures, since the choices degrade both the DOA and range estimation performance. We can clearly see the trade-off relationship between the DOA and range estimation performance.

Finally, we evaluate the empirical computational complexity of the proposed algorithm, the MUSIC based algorithm [8] and the 2D ANM algorithm

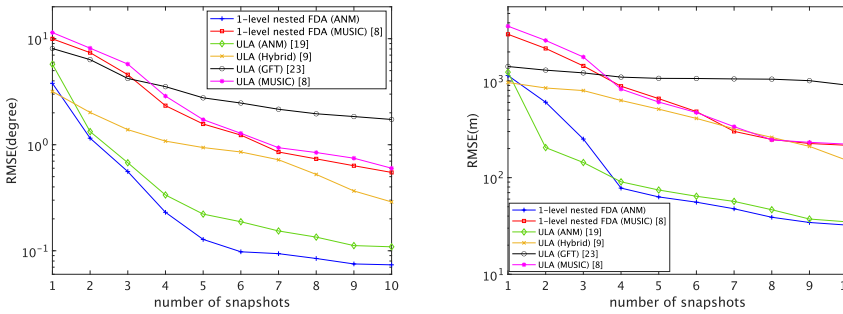

(a) DOA estimation. (b) Range estimation.

Figure 11: RMSE versus number of snapshots with coherent targets ($N = 10$).

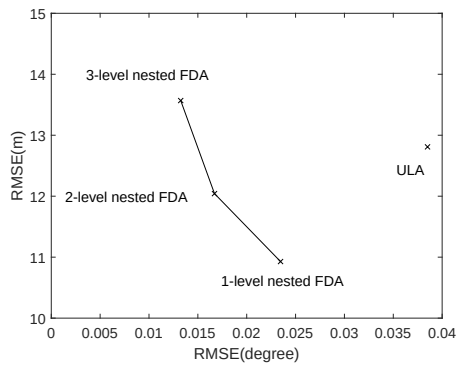

Figure 12: DOA and range RMSE performance trade-off ($N = 10$).

with ULA [19] in terms of the average computation time for DOA and range estimation in computer simulations. Note that, based on the discussion in Section 6, we focus our numerical comparison on the 2D ANM algorithm and the MUSIC based algorithm, as the MUSIC based algorithm requires the lowest theoretical computational complexity among the compared algorithms. The simulation environment is as follows: CPU: Intel Core i9-13900KF (number of cores: 24, base clock frequency: 3.0 GHz), memory: 64 GB, MATLAB version: 2023a, and OS version: Debian 6.1.106-3 x86_64 GNU/Linux. Figures 13a and 13b respectively show the results with the number of physical antennas $N = 6$ and 10 under SNR of 20 dB. As depicted in the figures, the average computation time of the proposed 2D ANM algorithm is greater than that of the MUSIC based algorithm. Thus, we can say that the proposed method achieves good estimation performance at the cost of higher compu-

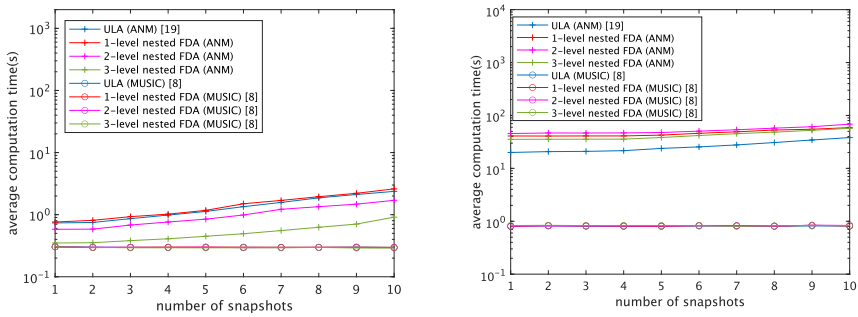

(a) Number of physical antennas $N = 6$. (b) Number of physical antennas $N = 10$.

Figure 13: Average computation time versus number of snapshots.

tational complexity. It should also be noted that in the proposed algorithm, the computation time depends on the level of the nested array, since the size of the matrix $\mathbf{T}(\boldsymbol{u})$ depends on it. With the fact that the proposed method achieves better estimation accuracy in the region of a small number of snapshots, the proposed method would be suited for applications, where a small number of snapshots is required.

8 Conclusion

In this paper, we have proposed to employ the nested array for the physical antenna array of the co-located FDA MIMO radar using the 2D ANM approach, where the inner ULA serves as the transmitting array, while whole nested array is utilized for the receiving array. Unlike the conventional approach of using the nested array solely for DOA estimation, the maximization of the virtual array aperture is not necessarily the best strategy for the case with the MIMO radar because it could result in the degradation of the range estimation performance. Thus, we have proposed to control the level of the nested array to take balance between DOA and range estimation performance. The effectiveness of the proposed approach is demonstrated via computer simulations comparing its performance with that of the conventional FDA MIMO radar using ULA and CRLBs.

Our future work includes the investigations of the estimation method, which can cope with the transmitting array taking advantage of the entire physical antenna array, and the computational complexity reduction scheme based on some grid-free approaches, which do not require the SDP solver. In addition, we plan to explore the applications of the proposed method in practical radar scenarios where fast response is critical, such as automotive radar

[21], UAV-based surveillance [17], and cognitive radar systems [7]. These environments typically involve rapid target or platform motion and dynamically changing conditions, under which the ability to perform accurate estimation with a small number of snapshots is particularly advantageous.

A Derivation of Received Signal After Matched Filtering

The matched filter output corresponding to the k-th target at the p-th receiving antenna originally transmitted from the m-th transmitting antenna is expressed as

$$\begin{aligned}\bar{y}_{m,p,k}(\tau) &= \int_0^T \phi_m^*(t-\tau)\,\hat{y}_{m,p,k}(t)dt. \\ &= \int_0^T \phi_m^*(t-\tau)\,e^{-j2\pi(f_0+\alpha_m\Delta f)t}x_{p,k}(t)dt \\ &= \int_0^T \phi_m^*(t-\tau)\,e^{-j2\pi(f_0+\alpha_m\Delta f)t}\sum_{m'=0}^{M-1}x_{m',p,k}(t)dt.\end{aligned}$$

$$\begin{aligned}&= \int_0^T \phi_m^*(t-\tau)\,e^{-j2\pi(f_0+\alpha_m\Delta f)t} \\ &\quad\cdot\sum_{m'=0}^{M-1}\phi_{m'}(t-\tau_{m',p,k})e^{j2\pi(f_0+\alpha_{m'}\Delta f)\left(t-\tau_{m',p,k}\right)}dt \\ &= \int_0^T \phi_m^*(t-\tau) \\ &\quad\cdot\sum_{m'=0}^{M-1}\phi_{m'}(t-\tau_{m',p,k})e^{j2\pi(\alpha_{m'}-\alpha_m)\Delta ft}e^{-j2\pi(f_0+\alpha_{m'}\Delta f)\tau_{m',p,k}}dt \\ &= \sum_{m'=0}^{M-1}e^{-j2\pi(f_0+\alpha_{m'}\Delta f)\tau_{m',p,k}} \\ &\quad\cdot\int_0^T \phi_m^*(t-\tau)\,\phi_{m'}(t-\tau_{m',p,k})e^{j2\pi(\alpha_{m'}-\alpha_m)\Delta ft}dt. \qquad (49)\end{aligned}$$

If we assume that $e^{j2\pi(\alpha_{m'}-\alpha_m)\Delta ft}$ has a constant value of $e^{j2\pi(\alpha_{m'}-\alpha_m)\frac{\Delta fT}{2}}$ for the range $t\in[0,T]$ due to the low frequency of Δf, the output of the matched filter can be approximated as

$$\bar{y}_{m,p,k}(\tau) \approx \sum_{m'=0}^{M-1} e^{-j2\pi(f_0+\alpha_{m'}\Delta f)\tau_{m',p,k}} e^{j2\pi(\alpha_{m'}-\alpha_m)\frac{\Delta f T}{2}} \cdot \int_0^T \phi_m^*(t-\tau)\,\phi_{m'}(t-\tau_{m',p,k})dt. \tag{50}$$

B Vandermonde Decomposition of Twofold Block Toeplitz Matrix

An $AB \times AB$ twofold block Toeplitz matrix $\mathbf{T}$ with rank K has its Vandermonde decomposition as [30]

$$\mathbf{T} = \mathbf{U}\boldsymbol{\Lambda}\mathbf{U}^H, \tag{51}$$

where $\boldsymbol{\Lambda}$ is a diagonal matrix and $\mathbf{U}$ is a block Vandermonde matrix expressed as

$$\mathbf{U} = \begin{bmatrix} 1\boldsymbol{f}_0 & \cdots & 1\boldsymbol{f}_{K-1} \\ e^{j2\pi l_0}\boldsymbol{f}_0 & \cdots & e^{j2\pi l_{K-1}}\boldsymbol{f}_{K-1} \\ \vdots & \ddots & \vdots \\ e^{j2\pi(A-1)l_0}\boldsymbol{f}_0 & \cdots & e^{j2\pi(A-1)l_{K-1}}\boldsymbol{f}_{K-1} \end{bmatrix}, \tag{52}$$

where $\mathbf{F} = [\boldsymbol{f}_0, \boldsymbol{f}_1, \cdots, \boldsymbol{f}_{K-1}] \in \mathbb{C}^{B\times K}$ denotes a Vandermonde matrix. If we define

$$\boldsymbol{l}_k = \left[1, e^{j2\pi l_k}, \cdots, e^{j2\pi(A-1)l_k}\right]^T, \tag{53}$$

the twofold block Toeplitz matrix $\mathbf{T}$ can be rewritten as

$$\mathbf{T} = (\mathbf{L} \odot \mathbf{F})\,\boldsymbol{\Lambda}\,(\mathbf{L} \odot \mathbf{F})^H, \tag{54}$$

where $\mathbf{L} = [\boldsymbol{l}_0, \boldsymbol{l}_1, \cdots, \boldsymbol{l}_{K-1}] \in \mathbb{C}^{A\times K}$. It is obviously found that $\mathbf{L}$ is also a Vandermonde matrix.

On the other hand, if we assume that a matrix $\mathbf{T} \in \mathbb{C}^{AB\times AB}$ admits a Vandermonde decomposition as

$$\mathbf{T} = (\mathbf{M} \odot \mathbf{G})\,\boldsymbol{\Gamma}\,(\mathbf{M} \odot \mathbf{G})^H, \tag{55}$$

where $\mathbf{M} \in \mathbb{C}^{A\times K}$ and $\mathbf{G} = [\boldsymbol{g}_0, \cdots, \boldsymbol{g}_{K-1}] \in \mathbb{C}^{B\times K}$ are Vandermonde matrices expressed as

$$\mathbf{M} = \begin{bmatrix} 1 & \cdots & 1 \\ e^{j2\pi m_0} & \cdots & e^{j2\pi m_{K-1}} \\ \vdots & \ddots & \vdots \\ e^{j2\pi(A-1)m_0} & \cdots & e^{j2\pi(A-1)m_{K-1}} \end{bmatrix}, \tag{56}$$

$$\mathbf{G} = \begin{bmatrix} 1 & \cdots & 1 \\ e^{j2\pi g_0} & \cdots & e^{j2\pi g_{K-1}} \\ \vdots & \ddots & \vdots \\ e^{j2\pi(B-1)g_0} & \cdots & e^{j2\pi(B-1)g_{K-1}} \end{bmatrix}, \tag{57}$$

and $\mathbf{\Gamma} \in \mathbb{C}^{K\times K}$ denotes a diagonal matrix with diagonal elements $\gamma_0, \gamma_1, \cdots, \gamma_{K-1}$.

Then, we have

$$(\mathbf{M} \odot \mathbf{G})\,\mathbf{\Gamma} = \begin{bmatrix} \gamma_0 \boldsymbol{g}_0 & \cdots & \gamma_{K-1}\boldsymbol{g}_{K-1} \\ \gamma_0 \boldsymbol{g}_0 e^{j2\pi m_0} & \cdots & \gamma_{K-1}\boldsymbol{g}_{K-1} e^{j2\pi m_{K-1}} \\ \vdots & \ddots & \vdots \\ \gamma_0 \boldsymbol{g}_0 e^{j2\pi(A-1)m_0} & \cdots & \gamma_{K-1}\boldsymbol{g}_{K-1} e^{j2\pi(A-1)m_{K-1}} \end{bmatrix},$$

and

$$(\mathbf{M} \odot \mathbf{G})^H = \begin{bmatrix} \boldsymbol{g}_0^H & \boldsymbol{g}_0^H e^{-j2\pi m_0} & \cdots & \boldsymbol{g}_0^H e^{-j2\pi(A-1)m_0} \\ \vdots & \vdots & \ddots & \vdots \\ \boldsymbol{g}_{K-1}^H & \boldsymbol{g}_{K-1}^H e^{-j2\pi m_{K-1}} & \cdots & \boldsymbol{g}_{K-1}^H e^{-j2\pi(A-1)m_{K-1}} \end{bmatrix}.$$

Thus, $\mathbf{T} = (\mathbf{M} \odot \mathbf{G})\,\mathbf{\Gamma}\,(\mathbf{M} \odot \mathbf{G})^H$ is a block matrix with each block size of $B \times B$, and the (p, q)-th block can be obtained as

$$\mathbf{T}_{(p,q)} = \sum_{k=0}^{K-1} \gamma_k \boldsymbol{g}_k \boldsymbol{g}_k^H e^{j2\pi m_k (p-q)}. \tag{58}$$

Since it depends only on $p - q$, we can confirm that $\mathbf{T}$ has a block Toeplitz structure. Moreover, the (s, t)-th element of $\mathbf{T}_{(\mathrm{p,q})}$ can be given by

$$\left(\mathbf{T}_{(p,q)}\right)_{(s,t)} = \sum_{k=0}^{K-1} \gamma_k e^{j2\pi m_k (p-q)} e^{j2\pi g_k (s-t)}, \tag{59}$$

and hence each block of $\mathbf{T}$ also has a Toeplitz structure, which confirms that the matrix $\mathbf{T}$ with the form in (55) is the twofold block Toeplitz matrix.

References

[1] P. Antonik, M. C. Wicks, H. D. Griffiths, and C. J. Baker, "Frequency diverse array radars", in *2006 IEEE Conference on Radar*, IEEE, 2006, 215–7.

[2] P.-H. Chou, B.-R. Zheng, W.-J. Huang, W. Saad, Y. Tsao, and R. Y. Chang, "Deep reinforcement learning-based precoding for multi-RIS-aided multiuser downlink systems with practical phase shift", *IEEE Wireless Communications Letters*, 14(1), January 2025, 23–7.

[3] C. Cui, J. Xu, R. Gui, W.-Q. Wang, and W. Wu, "Search-free DOD, DOA and range estimation for bistatic FDA-MIMO radar", *IEEE Access*, 6, 2018, 15431–45.

[4] D. L. Donoho, "Compressed sensing", *IEEE Transactions on information theory*, 52(4), April 2006, 1289–306.

[5] X. Duan, S. Zhu, L. Lan, X. Li, Y. Gao, and Y. Guo, "Joint range and angle estimation with coprime FDA-MIMO radar", in *IET International Radar Conference*, Vol. 2023, IET, 2023, 1218–24.

[6] Q. Feng, T. Tang, Z. Wu, Y. Zhang, and D. Wang, "A Deep Reinforcement Learning-based Shortwave Multistation Autonomous Cooperative Direction Finding and Localization Method", *IEEE Sensors Journal*, 2024.

[7] S. Z. Gurbuz, H. D. Griffiths, A. Charlish, M. Rangaswamy, M. S. Greco, and K. Bell, "An overview of cognitive radar: Past, present, and future", *IEEE Aerospace and Electronic Systems Magazine*, 34(12), 2020, 6–18.

[8] C. Hui, T. Xiang, L. Zihao, and J. Xinrui, "Reduced-dimension target parameter estimation for conformal FDA-MIMO radar", *Journal of Radars*, 10(6), December 2021, 811–21.

[9] S. M. Karbasi, "Angle-incremental range estimation for FDA-MIMO radar via hybrid sparse learning", *Digital Signal Processing*, 130(-), September 2022, 103749.

[10] C.-L. Liu and P. Vaidyanathan, "Super nested arrays: Linear sparse arrays with reduced mutual couplingPart I: Fundamentals", *IEEE Transactions on Signal Processing*, 64(15), 2016, 3997–4012.

[11] C.-L. Liu and P. Vaidyanathan, "Super nested arrays: Linear sparse arrays with reduced mutual couplingPart II: High-order extensions", *IEEE Transactions on Signal Processing*, 64(16), 2016, 4203–17.

[12] F. Liu, X. Wang, M. Huang, L. Wan, H. Wang, and B. Zhang, "A novel unitary ESPRIT algorithm for monostatic FDA-MIMO radar", *Sensors*, 20(3), February 2020, 827–44.

[13] J. Liu, Y. Zhang, Y. Lu, S. Ren, and S. Cao, "Augmented nested arrays with enhanced DOF and reduced mutual coupling", *IEEE Transactions on Signal Processing*, 65(21), 2017, 5549–63.

[14] Z.-Q. Luo, W.-K. Ma, A. M.-C. So, Y. Ye, and S. Zhang, "Semidefinite relaxation of quadratic optimization problems", *IEEE Signal Processing Magazine*, 27(3), 2010, 20–34.

[15] Z. Mao, S. Liu, Y. D. Zhang, L. Han, and Y. Huang, "Joint DoA-Range Estimation Using Space-Frequency Virtual Difference Coarray", *IEEE Transactions on Signal Processing*, 70, 2022, 2576–92.

[16] P. Pal and P. P. Vaidyanathan, "Nested arrays: A novel approach to array processing with enhanced degrees of freedom", *IEEE Transactions on Signal Processing*, 58(8), August 2010, 4167–81.

[17] V. P. Riabukha, "Radar surveillance of unmanned aerial vehicles", *Radioelectronics and Communications Systems*, 63(11), 2020, 561–73.

[18] M. Secmen, S. Demir, A. Hizal, and T. Eker, "Frequency diverse array antenna with periodic time modulated pattern in range and angle", in *2007 IEEE Radar Conference*, IEEE, 2007, 427–30.

[19] W.-G. Tang, H. Jiang, and Q. Zhang, "Range-angle decoupling and estimation for FDA-MIMO radar via atomic norm minimization and accelerated proximal gradient", *IEEE Signal Processing Letters*, 27, 2020, 366–70.

[20] J. A. Tropp and A. C. Gilbert, "Signal recovery from random measurements via orthogonal matching pursuit", *IEEE Transactions on information theory*, 53(12), December 2007, 4655–66.

[21] C. Waldschmidt, J. Hasch, and W. Menzel, "Automotive radar From first efforts to future systems", *IEEE Journal of Microwaves*, 1(1), 2021, 135–48.

[22] C. Wang, Z. Li, and X. Zhang, "FDA-MIMO for joint angle and range estimation: unfolded coprime framework and parameter estimation algorithm", *IET Radar, Sonar & Navigation*, 14(6), April 2020, 917–26.

[23] H. Wang, K. Liao, N. Xie, H. Chen, and Q. Li, "An FDA-MIMO radar 2-D parameter estimation algorithm based on graph signal processing", *Remote Sensing Letters*, 16(2), December 2024, 211–9.

[24] J. Wei, Y. Wei, L. Yu, and R. Xu, "Radar anti-jamming decision-making method based on DDPG-MADDPG algorithm", *Remote Sensing*, 15(16), 2023, 4046.

[25] X. Wu, Y. Liu, and X. Jia, "Gridless Target Localization for FDA-MIMO Radar with Sparse Arrays", in *2023 IEEE International Conference on Acoustics, Speech and Signal Processing*, IEEE, 2023, 1–5.

[26] J. Xiong, W.-Q. Wang, and K. Gao, "FDA-MIMO radar range–angle estimation: CRLB, MSE, and resolution analysis", *IEEE Transactions on Aerospace and Electronic Systems*, 54(1), February 2018, 284–94.

[27] Y. Yan, J. Cai, and W.-Q. Wang, "Two-stage ESPRIT for unambiguous angle and range estimation in FDA-MIMO radar", *Digital Signal Processing*, 92(-), September 2019, 151–65.

[28] Y. Yang, Z. Chu, and G. Ping, "Two-dimensional multiple-snapshot grid-free compressive beamforming", *Mechanical Systems and Signal Processing*, 124(-), June 2019, 524–40.

[29] Z. Yang and L. Xie, "Exact joint sparse frequency recovery via optimization methods", *IEEE Transactions on Signal Processing*, 64(19), October 2016, 5145–57.

[30] Z. Yang, L. Xie, and P. Stoica, "Vandermonde Decomposition of Multilevel Toeplitz Matrices With Application to Multidimensional Super-Resolution", *IEEE Transactions on Information Theory*, 62(6), June 2016, 3685–701.

[31] T. Zhang, F. Xu, and S. A. Vorobyov, "Transmit Energy Focusing For Parameter Estimation in Transmit Beamspace Slow-Time MIMO Radar", in *2023 IEEE International Conference on Acoustics, Speech and Signal Processing*, IEEE, 2023, 1–5.

[32] H. Zhao, H. Song, R. Liu, J. Hou, and X. Yu, "Anti-Jamming Decision-Making for Phased-Array Radar Based on Improved Deep Reinforcement Learning", *Electronics*, 14(11), 2025, 2305.